

Realization of narrowband thermal emission with optical nanostructures

TAKUYA INOUE,^{1,*} MENAKA DE ZOYSA,¹ TAKASHI ASANO,¹ AND SUSUMU NODA^{1,2}

¹Department of Electronic Science and Engineering, Kyoto University, Kyoto 615-8510, Japan

²e-mail: snoda@kuee.kyoto-u.ac.jp

*Corresponding author: t_inoue@qoe.kuee.kyoto-u.ac.jp

Received 23 July 2014; revised 2 December 2014; accepted 2 December 2014 (Doc. ID 217658); published 14 January 2015

The control of thermal emission spectra using optical resonances has been attracting increased attention both with respect to fundamental science and for various applications, including infrared sensing, thermal imaging, and thermophotovoltaics. In this mini-review, we describe the recent experimental demonstrations of narrowband thermal emission with optical nanostructures, including metallic cavities, metamaterials, and all-dielectric photonic crystals. The spectral features of the controlled thermal emission (e.g., wavelength, linewidth, peak emissivity, and angular characteristics) are strongly dependent on the choice of both materials and structures of the emitters. Through the appropriate design of optical nanostructures, arbitrary shaping of thermal emission spectra, from single-peak ultra-narrowband ($Q > 100$) emission for midinfrared sensing to a stepwise emissivity spectrum for thermophotovoltaics, has been successfully realized. © 2015 Optical Society of America

OCIS codes: (160.3900) Metals; (230.5590) Quantum-well, -wire and -dot devices; (300.6340) Spectroscopy, infrared; (350.5610) Radiation; (160.3918) Metamaterials; (230.5298) Photonic crystals.

<http://dx.doi.org/10.1364/OPTICA.2.000027>

1. INTRODUCTION

Thermal emitters generally exhibit a broad spectrum determined by Planck's law, and are used for various applications over a very wide range of frequencies. Midinfrared thermal emission is an important tool for nondispersive infrared (NDIR) sensing [1–4], since most gases and liquids show unique absorption spectra based on their molecular vibrations in this spectral range. Near-infrared and visible thermal emission is not only used for lighting applications, but is also converted to electrical power by solar cells, which is known as thermophotovoltaic power generation [5–10]. However, for any given application, only a narrow region spectrum is utilized. For example, the spectral range required for NDIR sensing is as narrow as the absorption linewidths of the target substances, typically corresponding to a Q factor [the ratio of a resonant frequency to the full width at half-maximum (FWHM) of its spectral peak] of more than 50 [11]. In the case of thermophotovoltaic power generation, thermal emission in a frequency range below the bandgap of the

photovoltaic cell passes through the cell without being absorbed, leading to the reduction of the power conversion efficiency. Therefore, there is a strong motivation to realize narrowband thermal emission with high emissivity (the ratio of the thermal emission intensity from an object to that from a blackbody) at a target wavelength while suppressing it as much as possible at all other wavelengths.

The principle of thermal emission control is based on Kirchhoff's law of thermal radiation [12], which states that the emissivity of an object is equal to the absorptivity for a given frequency, direction, and polarization. Therefore, in order to realize a narrowband thermal emission spectrum, we have to maximize the absorptivity of the emitter only at a target wavelength while minimizing it at all other wavelengths. One approach for obtaining narrowband absorptivity (emissivity) is the direct use of materials such as rare earth oxides, which inherently cause strong absorption at fixed wavelengths [13,14]. However, this approach does not allow us the arbitrary control of an emission wavelength or an emission bandwidth. On the

other hand, absorptivity is also dependent on the magnitude of interaction between light and materials. One can increase absorptivity at a particular wavelength by preparing an optical resonance, which enhances the light–matter interaction at that wavelength. Based on this concept, various types of wavelength-scale optical nanostructures have been utilized for thermal emission control in the past decades. Thermal emitters based on metallic nanostructures [6,7,9,15–24] have been most intensively investigated, where optical resonant modes confined in the microcavities or surface plasmon polaritons excited on the metal surface enhance the absorptivity (emissivity) at those resonant wavelengths. Since metals are stable even at high temperatures and show larger absorption in the near-infrared than at the longer wavelengths, they are potentially suitable for near-infrared selective thermal emitters in thermophotovoltaic applications. As a different approach, metamaterials which combine subwavelength metallic elements with thin dielectric layers have also realized narrowband thermal emission [25–32]. By properly designing the structure of each resonant element, one can artificially control the effective permittivity and permeability of the entire structure [33], leading to perfect absorption [34–36] (maximum emission) at the resonant wavelength. It should be noted, however, that strong free carrier absorption due to the metals in these two types of thermal emitters also leads to undesired emission over an extensive wavelength range and broadening of the emission peaks ($Q < 10$).

On the other hand, all-dielectric thermal emitters are promising for obtaining a narrower thermal emission peak with less background emission. The use of surface-phonon polariton resonances in polar materials [37–39] is one example; however, the emission wavelength cannot be tuned over a wide range because such resonances require strong lattice absorption, which is an intrinsic property of the material used. For the full control of a thermal emission spectrum in an arbitrary frequency range, it is necessary to use more tunable absorbing materials, where the frequency, bandwidth, and magnitude of absorption can be arbitrarily controlled such that these properties can be better combined with resonances in optical nanostructures. The use of an intersubband transition (ISB-T) [40] in doped semiconductor quantum wells has recently been proposed [41] in order to meet this challenge, and single-peak ultranarrowband ($Q > 100$) thermal emitters combining ISB-Ts in multiple quantum wells (MQWs) and photonic crystal slabs have been experimentally demonstrated [42–45].

In this work, we review the recent demonstrations of narrowband thermal emission with optical nanostructures. Our discussion mainly focuses on the spectral features of metallic and dielectric thermal emitters and their potential applications. In Section 2, we review the underlying physics and spectral characteristics of thermal emitters based on metallic nanostructures and metamaterials. In Section 3, thermal emission control with all-dielectric nanostructures are discussed, where we especially focus on the use of ISB-Ts in MQWs. In the conclusion, we discuss the future outlook of thermal emission control with optical nanostructures.

2. THERMAL EMISSION CONTROL BY METALLIC NANOSTRUCTURES AND METAMATERIALS

A. Metallic Nanostructures

Metallic nanostructures have been long utilized for the control of a thermal emission spectrum. They include three-dimensional (3D) photonic crystals [6,15], 2D photonic crystals [9,16–18], 2D microcavity arrays [7,19–21], and 1D surface gratings [22–24]. Metallic photonic crystals possess a large photonic bandgap, which suppresses thermal emission below the cutoff frequency. Meanwhile, resonant modes at the photonic band edges enhance the light–matter interaction, leading to strong narrowband absorption (or thermal emission). Metallic microcavity arrays exhibit similar spectra, where two-dimensionally confined electromagnetic modes inside the microcavities yield selective thermal emission. These spectral features are potentially suitable for selective emitters used in thermophotovoltaic applications. Refractory metals such as Tungsten (W) and Tantalum (Ta) are often chosen for emitter material since they show good thermal stability even at temperatures higher than 1000 K.

Figure 1(a) shows an example of a thermal emitter based on a 2D W microcavity array [21]. When the depth of the microcavity (d) is comparable to the aperture size (a), incident plane waves can couple to standing-wave resonances inside the cavity, leading to enhanced absorption in metals. The cutoff wavelength of the lowest-order mode is basically represented by $2a$, and thus one can control the cutoff wavelength of thermal emission by changing the aperture size of the microcavity. The scanning electron microscope image of a fabricated thermal emitter made of single crystalline W is shown in Fig. 1(b). The structure was fabricated by means of electron beam lithography and fast atom beam etching with SF_6 gas. Figure 1(c) shows the measured thermal emission spectrum of the fabricated W microcavity array and a flat W substrate at a temperature of 1180 K. The microcavity array shows enhanced thermal emission below the cutoff wavelength around $2\ \mu\text{m}$, while emission at longer wavelengths is kept as low as that of the flat metal substrate. The authors also reported the degradation of the spectral selectivity in the microcavities made of polycrystalline W, which was caused by the fast atomic diffusion at the grain boundaries.

Although single crystalline refractory metals show better spectral performances, thermal emitters based on polycrystalline metals are preferable in real applications due to their lower cost and easier availability. Figure 1(d) shows a selective thermal emitter based on a polycrystalline Ta photonic crystal with HfO_2 coatings for high-temperature applications [18]. The period, hole-radius, and hole-depth of the photonic crystal were optimized by the finite-difference time-domain (FDTD) method so that the best spectral selectivity below the target cutoff wavelength of $2\ \mu\text{m}$ can be obtained. A thin layer of 20 nm HfO_2 on the surface of photonic crystal suppresses surface diffusion, leading to grain boundary grooving. The measured emissivity spectra show strong thermal emission below the cutoff wavelength with lower emission at longer wavelength ($\lambda > 3\ \mu\text{m}$), which agrees well with the simulation result. Since photonic crystals with deep air holes support

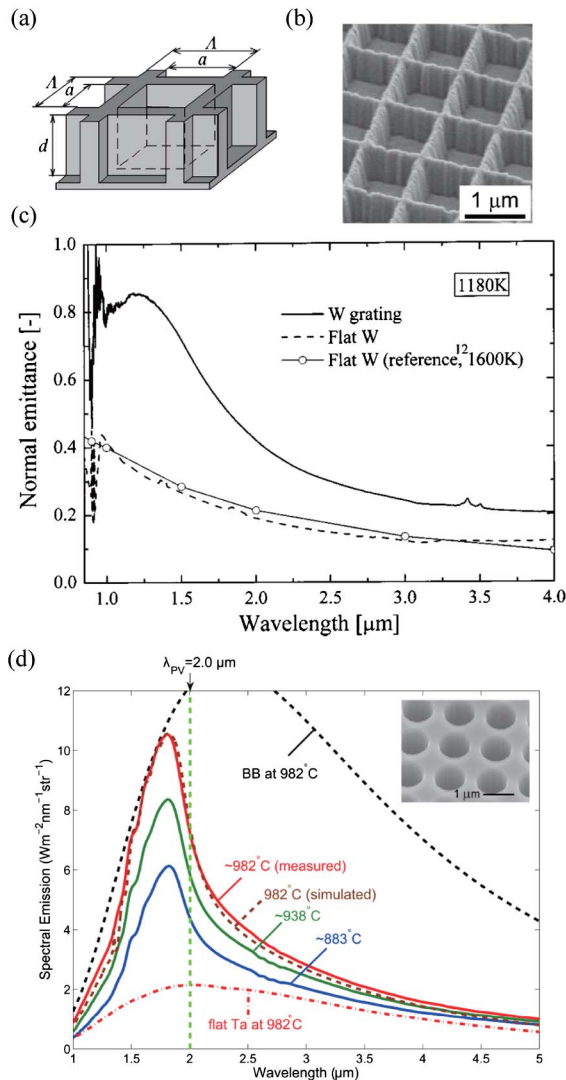


Fig. 1. (a) Schematic of a 2D array of rectangular metallic microcavities for thermal emission control. (b) Scanning electron micrograph (SEM) image of a fabricated emitter made of single crystalline W with $\Lambda = 1.0 \mu\text{m}$, $a = 0.8 \mu\text{m}$, and $d = 0.8 \mu\text{m}$. (c) Measured normal emissivity spectrum of the 2D array of microcavities and a flat W substrate at 1180 K. The solid line with circles represents a reported emissivity spectrum of flat W. (d) Thermal emission spectra of a polycrystalline Ta photonic crystal with HfO_2 coating at different temperatures (solid lines), compared to the simulated emission of a Ta photonic crystal (dashed line), calculated emission of flat Ta (dashed-dotted line), and calculated blackbody emission (dashed black line) at 982°C. The inset shows a SEM image of the fabricated Ta photonic crystal. (a)–(c) reprinted from Ref. [21] with permission from AIP Publishing LLC (2003); (d) reprinted from Ref. [18], Copyright Optical Society of America (2013).

multiple higher-order band edge resonant modes, the emission spectra do not show individual sharp emission peaks but exhibit a continuous emission “band” below the cutoff wavelength. Such stepwise emission spectra can be better matched to an absorption band of small-bandgap solar cells such as GaSb and InGaAsSb, which is a key for highly efficient thermal-to-electrical energy conversion in thermophotovoltaics [5–10].

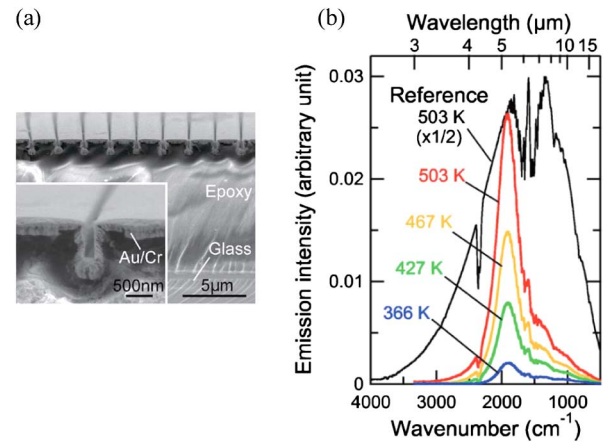


Fig. 2. (a) SEM image of a fabricated Au/Cr grating. (b) Measured TM-polarized emission spectra from a grating with period of $2.99 \mu\text{m}$, width of 316 nm , and depth of $1.04 \mu\text{m}$. The thermal emission spectrum of the reference blackbody sample at 503 K is also shown. Reprinted from Ref. [22] with permission from AIP Publishing LLC (2008).

1D metallic gratings with narrower widths or shallower depths [22–24] show different thermal emission characteristics. Such metallic gratings efficiently couple surface plasmon polaritons at the interface between metals and dielectrics (e.g., air) to radiative thermal emission. Unlike the case of 2D/3D photonic crystals and microcavities, they show linearly polarized thermal emission due to the transverse magnetic (TM)-polarized nature of surface plasmon polaritons. Figure 2(a) shows an example of the fabricated 1D metallic grating and Fig. 2(b) shows its TM-polarized thermal emission spectra [22]. A narrowband emission peak with a quality factor of around 5 is obtained in the midinfrared range, while higher-order resonances at shorter wavelengths are filtered out by the Planck distribution at a moderately high temperature (503 K). By employing orthogonal component gratings with different periods, orthogonally polarized midinfrared emission with different wavelengths was also demonstrated [23], which may have such potential applications as chemical analysis and gas sensing.

B. Metamaterials

Metamaterials are arrays of subwavelength resonant elements (typically made of metals) combined with thin dielectric layers, where the electric permittivity $\epsilon(\omega)$ and magnetic permeability $\mu(\omega)$ of the entire medium can be artificially controlled by the design of each resonant element. By matching the impedance of the metamaterial $Z(\omega) = [\mu(\omega)/\epsilon(\omega)]^{1/2}$ to that of free space, one can minimize the reflectivity and achieve perfect absorption [34–36] (a review for metamaterial absorbers is provided in Ref. [46]). According to Kirchhoff’s radiation law, perfect absorption means thermal emission with an emissivity of 1. Since the resonant wavelength can be easily tuned by changing the shape, size, and material composition of each subwavelength element, one can obtain a strong narrowband thermal emission peak at an arbitrary wavelength.

Despite its relatively short history, the use of metamaterials in thermal applications is attracting increasing attention these

days due to their greater design flexibility [25–32]. Most thermal emitters employ a metal–insulator–metal (MIM) configuration, where the upper metal layer consists of an array of disconnected metal patches. Such disconnection converts propagating plasmon modes in a usual MIM waveguide to localized plasmon resonances with strongly localized electromagnetic fields in the subwavelength dielectric spacer [25], which effectively modify $\epsilon(\omega)$ and $\mu(\omega)$ (and the absorptivity spectrum) of the structure [35]. Since spatially localized electromagnetic fields contain broad Fourier components in the wavenumber space, metamaterial-based thermal emitters exhibit angle-insensitive thermal emission spectra [27,28,31]. Furthermore, the localization of electromagnetic fields also enables the compaction of multiple resonant elements in a single-unit cell, which realizes dual-band or multiband thermal emission [26,32]. Figure 3 shows one example of midinfrared narrowband thermal emitters based on a MIM structure [26]. The left panel in Fig. 3(a) shows a schematic of a single-band thermal emitter, which consists of a cross-shaped gold resonator, a dielectric spacer (benzocyclobutene), and a gold ground plane. The resonant wavelength of the cross resonator is proportional to its length. Since this structure is invariant under rotations of 90°, it generates polarization-insensitive thermal emission. By integrating two different cross resonators to form a checkerboard-like unit cell as shown in the right panel of Fig. 3(a), one can construct a dual-band narrowband thermal emitter (a dielectric spacer of Al_2O_3 is used). Fabrication of these metamaterials can be done using lithography and lift-off techniques, which do not require a dry etching process of hard metals. Figure 3(b) shows the experimental emissivity spectra of the single-band (left) and dual-band (right) thermal emitters at five different temperatures from 100°C to 300°C. The single-band emitter yields a thermal emission peak with an emissivity as high as 0.98 at a wavelength of 5.8 μm . The

dual-band emitter also shows two emission peaks whose emissivities are 0.85 and 0.89, respectively. The Q factors of these peaks are around 10. These results clearly indicate the usability of metamaterials for narrowband thermal emitters.

As an approach for more direct control of the electric permittivity $\epsilon(\omega)$ and magnetic permeability $\mu(\omega)$, a multilayer structure composed of alternating layers of metal and dielectric shown in Fig. 4(a) has been theoretically investigated [30]. When the thickness of each layer is much thinner than the target wavelength, this structure can be regarded as an effective medium whose electric permittivity (for in-plane and vertical directions) is given by

$$\epsilon_{\parallel} = \epsilon_M \rho + \epsilon_D(1 - \rho) \quad \epsilon_{\perp} = \frac{\epsilon_M \epsilon_D}{\epsilon_M(1 - \rho) + \epsilon_D \rho}, \quad (1)$$

where ϵ_M and ϵ_D are permittivity of the metallic and the dielectric layers, respectively, and ρ is the relative fill factor of the metal in the unit cell. In the infrared regime, the real part of ϵ_M usually takes a negative value while that of ϵ_D is positive, and one can artificially adjust these parameters to near zero by choosing the appropriate fill factor ρ . Such an “epsilon-near-zero” medium shows increased absorption because the displacement field boundary condition ($\epsilon_1 E_{1\perp} = \epsilon_2 E_{2\perp}$) yields a strong electric field enhancement ($E_{2\perp} \rightarrow \infty$) if $\epsilon_2 \rightarrow 0$. Figure 4(b) shows a calculated emissivity spectrum of the multilayer metamaterial. The structure exhibits strong thermal emission owing to the above mechanism below the wavelength of 1.5 μm , where the real part of ϵ_{\parallel} crosses zero (shown in the inset). Above that wavelength, the real part of ϵ_{\parallel} takes a negative value far from zero and the medium behaves like metal, which shows high reflectivity at the longer wavelengths. Such spectral selectivity is suitable for thermophotovoltaic applications as described in the previous subsection. It should be noted, however, that the multilayer structure composed of two different materials (metal and dielectric) might be degraded easily at high temperature.

C. Discussion

As described in the previous two subsections, metallic nanostructures and metamaterials have successfully modified

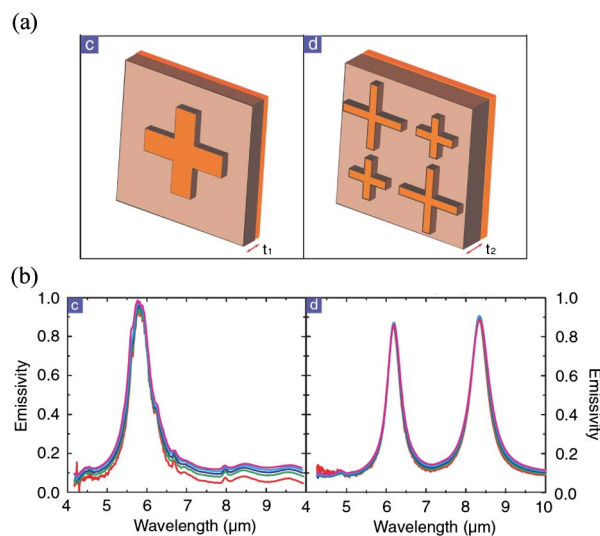


Fig. 3. (a) Schematic of single-band (left) and dual-band (right) infrared metamaterial thermal emitters. (b) Measured emissivity spectra of fabricated single-band (left) and dual-band (right) metamaterial thermal emitters at five different temperatures. Reprinted from Ref. [26] with permission from American Physical Society (2011).

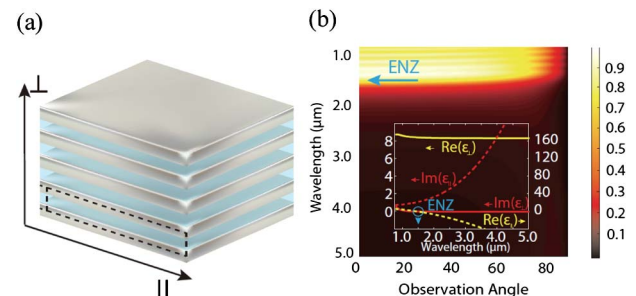


Fig. 4. (a) Schematic of a multilayer metamaterial composed of alternating layers of metal and dielectric. (b) Calculated emissivity of a planar multilayer structure. The metamaterial is composed of 20 unit cells of 5 nm thick tantalum (modeled by a Drude relation) and 45 nm of titanium dioxide on optically thick tantalum substrate. The inset shows the effective medium parameters as functions of wavelength. Reprinted from Ref. [30] with permission from Optical Society of America (2012).

thermal emission spectra. By choosing the appropriate type of nanostructure, one can control the form of thermal emission spectra (from single-peak to multiband), the polarization (linearly polarized or polarization-insensitive), and the emission wavelength (from the near-infrared to the midinfrared). One drawback of metallic thermal emitters and metamaterials is their undesired nonzero emission over an extensive wavelength range (see the emission spectra shown in Figs. 1–3). This is due to strong free carrier absorption of metal layers. Such broadband emission degrades the performance of thermal emitters, for example, which reduces the achievable power conversion efficiency in thermophotovoltaic systems. Furthermore, strong absorption of metals also leads to the broadening of thermal emission peaks at the resonant wavelengths. The Q factors of the emission peaks are usually less than 10, which is not suitable for many applications requiring much narrower thermal emission peaks. To overcome these limitations, thermal emission control without metals is desirable. In the next section, we focus on all-dielectric optical nanostructures for much narrower thermal emission.

3. THERMAL EMISSION CONTROL BY ALL-DIELECTRIC NANOSTRUCTURES

A. Choice of Materials

As described in the introduction, the important first step toward obtaining narrowband thermal emission with suppressed background emission is the choice of materials which exhibit strong absorption around a target wavelength and negligibly small absorption at all other wavelengths. Dielectric materials which are transparent in a wide range of frequencies (e.g., undoped Si and GaAs) are better platforms than metals in this respect, since they emit little background thermal emission. The point is how to create absorption only at the target wavelength. One approach is the use of the Reststrahlen band, where strong absorption occurs as a result of the interaction between light and phonon modes inside the polar materials such as SiC and GaP. By combining these materials with surface gratings, one can obtain narrowband absorption assisted by surface phonon polaritons [37–39]. Figure 5 shows experimental and theoretical reflectivity spectra of a 1D grating made of SiC for different observation angles [37]. The grating period ($6.25\ \mu\text{m}$) is chosen so that a surface wave, which exists only in the Reststrahlen band of SiC ($\lambda = 10\text{--}12.5\ \mu\text{m}$), can be coupled to a propagating wave from/to the far field. Sharp absorption dips are observed at $\lambda = 11.0\ \mu\text{m}$ and $\lambda = 11.4\ \mu\text{m}$ at the observation angles of 30° and 45° , respectively, owing to the excitation of surface phonon polaritons. The FWHMs of these dips are quite narrow, corresponding to Q factors of 50–100. When the sample was heated to 773 K, highly directional thermal emission at the wavelength corresponding to the absorption dips was observed (not shown).

The use of MQWs is another promising approach because an electronic transition between two quantized energy levels in the conduction band, known as an ISB-T, gives rise to a narrowband absorption peak with typical FWHMs of $50\ \text{cm}^{-1}$ to $100\ \text{cm}^{-1}$ [40]. By properly modifying the well width, barrier height, and materials, the ISB-T wavelength can be tuned over

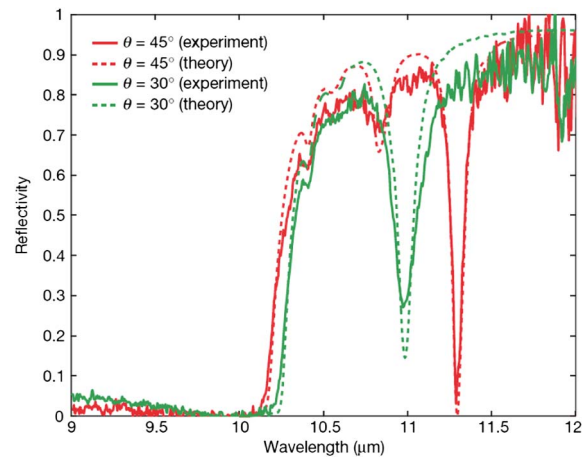


Fig. 5. Measured (solid) and calculated (dashed) reflectivity spectra of a SiC grating at room temperature for different observation angles 30° (green) and 45° (red). The incident light is TM-polarized. Reprinted from Ref. [37] with permission from Macmillan Publishers Ltd: Nature (London) (2002).

a wide range from the THz to near-infrared region [47,48]. Furthermore, the magnitude of the absorption coefficient at the transition wavelength can be controlled by changing the doping density, which is useful for obtaining a thermal emission peak with a high Q factor and high emissivity (this advantage is discussed in detail later).

Figure 6(a) shows a schematic of MQWs used for the control of thermal emission [42]. The sample consists of

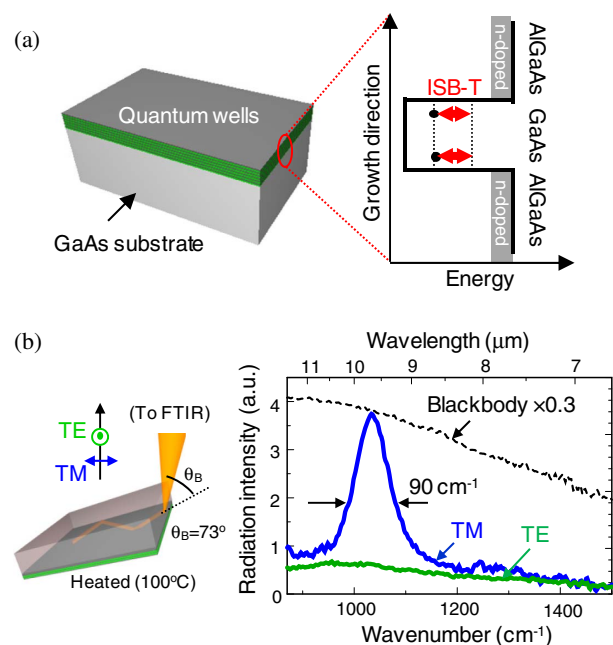


Fig. 6. (a) Schematic of ISB-Ts in multiple quantum wells used for control of thermal emission. (b) Thermal emission spectra of the quantum wells at 100°C for transverse-magnetic (TM) and transverse-electric (TE) polarization. The optical setup is shown schematically in the left panel, where θ_B denotes Brewster's angle of GaAs. The dashed line shows the emission spectrum of a blackbody reference. Reprinted from Ref. [42].

63 periods of 6.8 nm thick GaAs quantum wells and 13-nm-thick $\text{Al}_{0.3}\text{Ga}_{0.7}\text{As}$ barriers doped with silicon at a density of $1.0 \times 10^{17} \text{ cm}^{-3}$ on a GaAs semi-insulating substrate. Figure 6(b) shows the thermal emission spectrum of the sample when heated to 100°C. Thermal emission was measured from the end facet of the sample at Brewster's angle of GaAs (θ_B) as shown in Fig. 6(b), because the ISB-T has TM polarization and does not emit normal to the sample surface. A narrowband thermal emission peak with a FWHM of 90 cm^{-1} at a wavelength of $9.7 \mu\text{m}$ is observed for TM polarization. The wavelength and FWHM of this peak agree well with those of the ISB-T absorption spectrum confirmed by transmission measurement. When this narrowband absorption (thermal emission) spectrum of the ISB-T is combined with optical resonances in a periodic nanostructure, a much narrower thermal emission peak with well-suppressed background can be achieved. In the next subsection, a detailed procedure for designing such single-peak ultra-narrowband thermal emitters is discussed along with the relevant experimental results.

B. Single-Peak Ultra-Narrowband Thermal Emitters based on ISB-Ts in MQWs and Photonic Crystal Slabs

Figure 7(a) shows a schematic of a thermal emitter in which MQWs are combined with a photonic crystal slab composed of a square lattice of rods [43]. Figure 7(b) shows the calculated photonic band diagram of this structure for resonant modes with TM-like polarization (=ISB-T polarization). By reducing the thickness of the emitter down to the wavelength scale, the number of guided modes is decreased. The lattice constant of the photonic crystal is adjusted so that one of the second-order band edge resonant modes at the Γ point [49,50] lies within the absorption bandwidth of the ISB-T of the MQWs, which yields thermal emission normal to the surface of the emitter. The rod structure employed here generally has a larger mode separation between these band edge resonant modes than the holey structure [51]. Since only one Γ point resonant mode exists within the absorption range of the ISB-T in Fig. 7(b), one can obtain single-peak thermal emission from this mode.

The upward emissivity spectrum obtained from this resonant mode is analytically expressed as

$$\varepsilon^U(\omega) = \frac{\xi}{1 + \xi} \times \frac{1/Q_{\text{abs}} Q_{\text{rad}}}{(\omega/\omega_{\text{res}} - 1)^2 + (1/2Q_{\text{abs}} + 1/2Q_{\text{rad}})^2}, \quad (2)$$

where ξ is the ratio between the upward and downward emission power, ω_{res} is the angular frequency of the resonant mode, and Q_{abs} , Q_{rad} are the Q factors of the resonant mode determined by the absorption of the material and by radiation to the surrounding space, respectively [43]. The total Q factor of the emissivity spectrum is given by $(Q_{\text{abs}}^{-1} + Q_{\text{rad}}^{-1})^{-1}$, which becomes high when both Q_{abs} and Q_{rad} are high [note that absorptive Q factor (Q_{abs}) is very low in the case of metallic nanostructures and metamaterials, leading to the broadening of the emission peaks]. The peak emissivity is maximized when the Q matching condition ($Q_{\text{abs}} = Q_{\text{rad}}$) is satisfied [41,52,53]. Therefore, if one can obtain full control over these

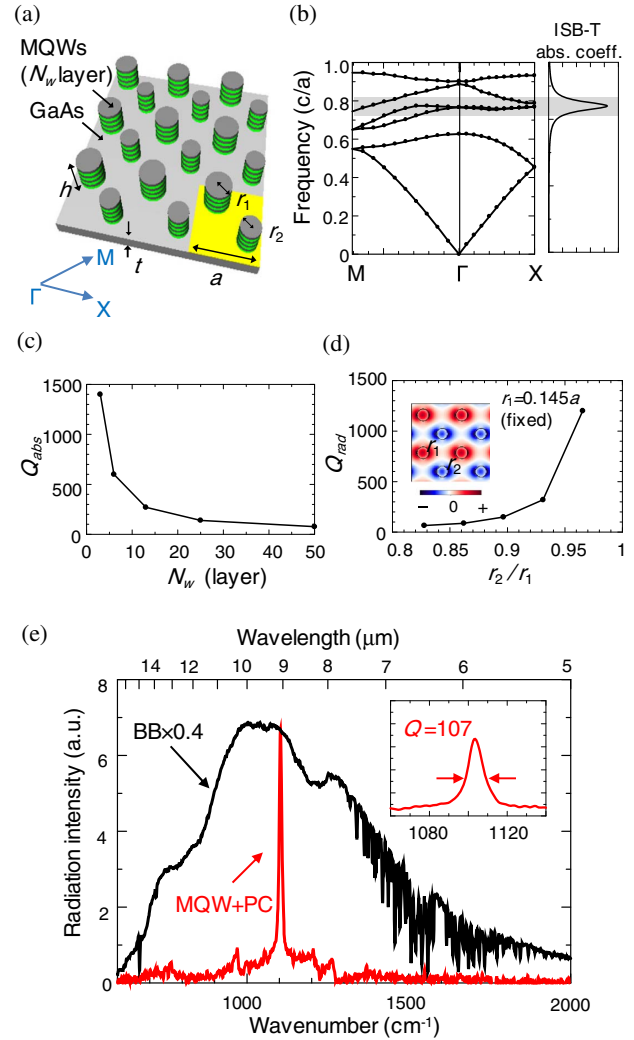


Fig. 7. (a) Structure of a single-peak, narrowband thermal emitter based on multiple quantum wells and a photonic crystal (PC) slab. The unit cell (marked in yellow) contains two rods with different radii. (b) Calculated photonic band diagram for the TM-like modes. The structural parameters for the calculation were set to $a = 7.0 \mu\text{m}$, $h = 2.6 \mu\text{m}$, $t = 0.6 \mu\text{m}$, $r_1 = 0.145a$, and $r_2 = 0.135a$. The position of the ISB-T absorption spectrum is shaded gray for reference. (c) Calculated Q factor of the Γ -point resonant mode in Fig. 7(b), determined by the intersubband absorption (Q_{abs}) as a function of the number of quantum well layers. An ISB-T absorption coefficient of 4200 cm^{-1} at the transition wavelength was assumed in the calculation. (d) Calculated Q factor of the same mode, determined by the far-field radiation (Q_{rad}), as a function of the ratio of the two rod radii (r_2/r_1). The inset shows the electric-field (E_x) distribution of the mode. (e) Measured thermal radiation intensity spectra of the fabricated emitter ($a = 7.6 \mu\text{m}$, $h = 1.3 \mu\text{m}$, $t = 0.6 \mu\text{m}$, $r_1 = 0.17a$, $r_2 = 0.15a$, and $N_w = 13$) and reference blackbody sample in the surface-normal direction at a temperature of 200°C. Reprinted from Refs. [43] and [44].

parameters (Q_{abs} , Q_{rad} , ξ), a thermal emission peak with an arbitrary linewidth and an emissivity close to 1 will be achieved. In the structure shown in Fig. 7(a), Q_{abs} can be readily controlled by changing the number of quantum wells [a decrease in the number of quantum wells leads to higher Q_{abs} as shown in Fig. 7(c)]. On the other hand, Q_{rad} can

be tuned by adjusting the ratio of the two radii (r_2/r_1) as shown in Fig. 7(d). This is possible because the radiation from the two rods partially cancels in the far field, as can be understood from the near-field pattern (E_x) at the Γ point shown in the inset of Fig. 7(d). The degree of cancellation is enhanced when r_2/r_1 approaches unity, which leads to a higher Q_{rad} . Adjustment of these two Q factors allows the Q matching condition ($Q_{\text{abs}} = Q_{\text{rad}}$) in the high- Q regime to be met. Equation (2) also suggests that, to maximize the emissivity in the upward surface direction, it is important to maximize the ratio between the upward and downward radiation ξ . Calculations reveal that when the height of the rods is optimized ($2.6 \mu\text{m}$), ξ becomes as large as 9, corresponding to the maximum upward emissivity of 0.9. The smaller rod height ($1.3 \mu\text{m}$) reduces the maximum emissivity to 0.7, but the fabrication by reactive ion etching becomes easier.

Figure 7(e) shows the measured thermal emission spectra of the fabricated emitter and a reference blackbody sample, where both devices were heated to 200°C using an external heater [44]. The photonic crystal emitter exhibits a narrowband emission peak at a wavelength of $9.1 \mu\text{m}$ with a Q factor of 107 and suppressed emission at all other wavelengths. Comparing to the blackbody reference spectrum, the peak emissivity of the narrowband emitter is 0.4 while the emissivity at off-peak wavelengths is much lower. The rather low peak emissivity results from a decreased ISB-T absorption coefficient (increase in Q_{abs}) during the fabrication process and a decrease in Q_{rad} caused by structural imperfections in the fabricated device, which leads to a mismatch between the values of Q_{abs} and Q_{rad} in Eq. (2). Higher peak emissivity will be achieved by improving the fabrication accuracy and adopting quantum wells with higher doping density in order to compensate for the reduction of the absorption coefficient.

As mentioned in the Introduction, one important application of narrowband thermal emitters is NDIR sensing of gases and chemical compounds. A typical NDIR sensing setup involves blackbody-like thermal emitters and narrowband optical filters whose passbands cover the absorption lines of the target substances [4]. However, such filters block most of the emission and thus lower the power utilization efficiency of the whole system. Instead, by using narrowband thermal emitters whose emission wavelengths are tuned to the target absorption lines, compact and highly efficient NDIR sensing systems will be realized. Such “filter-free” NDIR sensing has been recently demonstrated using the above ultra-narrowband thermal emitters [45], where the discrimination and concentration determination of three organic solvents (acetone, *o*-xylene, trichloroethylene) were successfully performed.

C. Discussion: Comparison between Metallic and All-Dielectric Thermal Emitters

As we have described in the previous subsections, all-dielectric thermal emitters exhibit a much narrower thermal emission peak with less background emission than metallic emitters show. These spectral features are beneficial in terms of the power utilization efficiency of the devices. In an ideal situation where no other significant power dissipation channels exist, all the power (heat) injected into a thermal emitter accumulates in

the form of phonons, increases the temperature of the device, and is then released as thermal emission within the designed range. Since the just-discussed all-dielectric thermal emitters radiate in a very narrow bandwidth (inversely proportional to the Q factor) with little background emission, it is expected that under the same input power conditions, the steady-state temperature of the emitters [which is determined by the equation of the input power with the total output power (including the dissipated power)] will become much higher than a blackbody emitter, leading to the peak thermal emission intensity greater than that of a blackbody. Such an “energy recycling” process has been experimentally demonstrated by using a MQW-PC thermal emitter with a different structure [42], and will contribute to the significant improvement of the power utilization efficiency of the entire system in various applications.

Another interesting aspect of all-dielectric thermal emitters is their dynamic controllability. Dynamic thermal emission control is highly desirable for a wide variety of applications, but has been a major challenge because the thermal emission intensity from an object is usually determined by its temperature, which is difficult to modulate quickly. However, if the emissivity (absorptivity) of the object is rapidly changed instead of the temperature, much faster control of thermal emission can be achieved. Unlike the case of metallic structures, whose optical properties are fixed once the structure is determined, the absorptivity (emissivity) of the all-dielectric narrowband thermal emitters based on ISB-Ts can be externally controlled by changing the carrier concentration in the MQWs. Based on this approach, voltage control of narrowband thermal emission has been recently demonstrated [54], where the electrons in the MQWs were electrically extracted/injected by using a p-n diode structure (Fig. 8). The modulation frequency of the emitter has reached $\sim 1 \text{ MHz}$, which is four orders of magnitude faster than that of conventional thermal emitters. Such high-speed control of thermal emission will further expand the potential applications of narrowband thermal emitters.

On the other hand, the maximum operating temperature of the all-dielectric narrowband thermal emitters demonstrated so far ($\sim 700 \text{ K}$) is lower than that of metallic structures

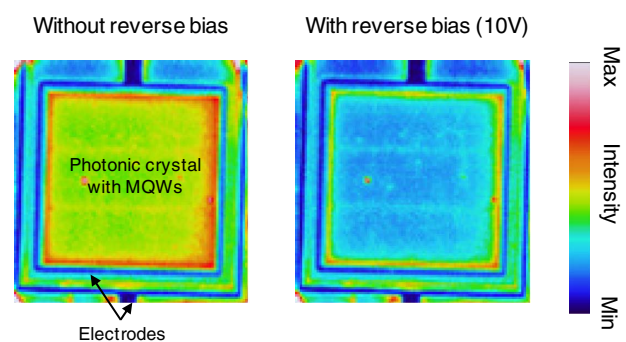


Fig. 8. Infrared camera image of the dynamically controllable narrowband thermal emitter (100°C) with and without reverse bias. When the reverse bias is applied, the electrons in the MQWs are extracted from the wells, leading to the decrease in the absorptivity (emissivity) of the device. Reprinted from Ref. [54].

(>1000 K), which prevents the realization of high-intensity thermal emission in the wavelengths shorter than 4 μm according to Wien's displacement law. For example, GaAs/AlGaAs quantum wells utilized in previous subsections will start to decompose when they are heated above their growth temperature (~ 800 K) in vacuum. Appropriate choice of dielectrics which have higher growth temperature will be able to raise the operating temperature of all-dielectric thermal emitters in the future. In contrast, metal-based thermal emitters, whose excellent stability at high temperature has been already demonstrated, seem to be more suitable for such high-temperature applications at the present time.

4. CONCLUSION AND PERSPECTIVES

In this review, we have shown that thermal emission spectra can be arbitrarily controlled by utilizing optical resonances in wavelength-scale periodic nanostructures. Metallic photonic crystals and microcavity arrays have successfully realized selective thermal emission in the near-infrared region at very high temperatures (>1000 K), which may greatly contribute to the increase of power conversion efficiency in thermophotovoltaic applications. Midinfrared narrowband thermal emitters based on metamaterials, which require much simpler fabrication process and yet possess greater design flexibility, have also been demonstrated. Ultra-narrowband ($Q > 100$), background-free thermal emission has been achieved by the combination of ISB-Ts of quantum wells with a dielectric photonic crystal slab, which will make expensive and cumbersome midinfrared optical components such as bandpass filters and monochrometers unnecessary in various applications, including infrared sensing and thermal imaging.

Although we have focused our discussion on the spectral control of thermal emission, the above nanostructures will enable much more fundamental control of thermal emission. Dynamic control of thermal emission discussed in Section 3.C is one example; by integrating multiple thermal emitters with different emission wavelengths and dynamically controlling the emission intensity of each emitter, an ultrafast wavelength scanning in the entire infrared range will be realized. Thermal emission control in the near field [55–60] is another hot topic; when two surfaces are brought very close to each other, not only propagating waves but also evanescent waves inside one object can tunnel to the other, leading to thermal emission exceeding Planck's blackbody radiation law. We believe that these fundamental demonstrations will further accelerate research toward the ultimate control of thermal emission in various fields of science.

FUNDING INFORMATION

Japan Science and Technology Agency (JST) (CREST); Japan Society for the Promotion of Science (JSPS) (Grant-in-Aid for JSPS Fellows, Grant-in-Aid for Scientific Research S (25220607)); Ministry of Education, Culture, Sports, Science, and Technology (MEXT) (Grants for Excellent Graduate Schools).

REFERENCES

1. J. Meléndez, A. J. de Castro, F. López, and J. Meneses, "Spectrally selective gas cell for electrooptical infrared compact multigas sensor," *Sens. Actuators A* **47**, 417–421 (1995).
2. P. Werle, F. Slemr, K. Maurer, R. Kormann, R. Mücke, and B. Jänker, "Near- and mid-infrared laser-optical sensors for gas analysis," *Opt. Lasers Eng.* **37**, 101–114 (2002).
3. R. Rubio, J. Santander, L. Fonseca, N. Sabaté, I. Gràcia, C. Cané, S. Udina, and S. Marco, "Non-selective NDIR array for gas detection," *Sens. Actuators B* **127**, 69–73 (2007).
4. J. Hodgkinson and R. P. Tatam, "Optical gas sensing: a review," *Meas. Sci. Technol.* **24**, 012004 (2013).
5. R. M. Swanson, "A proposed thermophotovoltaic solar energy conversion system," *Proc. IEEE* **67**, 446–447 (1979).
6. S. Y. Lin, J. Moreno, and J. G. Fleming, "Three-dimensional photonic-crystal emitter for thermal photovoltaic power generation," *Appl. Phys. Lett.* **83**, 380–382 (2003).
7. H. Sai and H. Yugami, "Thermophotovoltaic generation with selective radiators based on tungsten surface gratings," *Appl. Phys. Lett.* **85**, 3399–3401 (2004).
8. E. Rephaeli and S. Fan, "Absorber and emitter for solar thermophotovoltaic systems to achieve efficiency exceeding the Shockley–Queisser limit," *Opt. Express* **17**, 15145–15159 (2009).
9. W. R. Chan, P. Bermel, R. C. N. Pilawa-Podgurski, C. H. Marton, K. F. Jenson, J. J. Senkevich, J. D. Joannopoulos, M. Soljačić, and I. Celanovic, "Toward high-energy-density, high-efficiency, and moderate-temperature chip-scale thermophotovoltaics," *Proc. Natl. Acad. Sci. USA* **110**, 5309–5314 (2013).
10. A. Lenert, D. M. Bierman, Y. Nam, W. R. Chan, I. Celanovic, M. Soljačić, and E. N. Wang, "A nanophotonic solar thermophotovoltaic device," *Nat. Nanotechnol.* **9**, 126–130 (2014).
11. L. S. Rothman, I. E. Gordon, A. Barbe, D. C. Benner, P. F. Bernath, M. Birk, V. Boudon, L. R. Brown, A. Campargue, J.-P. Champion, K. Chance, L. H. Coudert, V. Dana, V. M. Devi, S. Fally, J.-M. Flaud, R. R. Gamache, A. Goldman, D. Jacquemart, I. Kleiner, N. Lacome, W. J. Lafferty, J.-Y. Mandin, S. T. Massie, S. N. Mikhailenko, C. E. Miller, N. Moazzen-Ahmadi, O. V. Naumenko, A. V. Nikitin, J. Orphal, V. I. Perevalov, A. Perrin, A. Predoi-Cross, C. P. Rinsland, M. Rotger, M. Simeckova, M. A. H. Smith, K. Sung, S. A. Tashkun, J. Tennyson, R. A. Toth, A. C. Vandaele, and J. Vander Auwera, "The HITRAN 2008 molecular spectroscopic database," *J. Quant. Spectrosc. Radiat. Transfer* **110**, 533–572 (2009).
12. D. B. Brace, *The Laws of Radiation and Absorption: Memoirs by Prévost, Stewart, Kirchhoff, and Kirchhoff and Bunsen* (American Book Company, 1901).
13. H. Sai, H. Yugami, K. Nakamura, N. Nakagawa, H. Ohtsubo, and S. Maruyama, "Selective emission of $\text{Al}_2\text{O}_3/\text{Er}_3\text{Al}_5\text{O}_{12}$ eutectic composite for thermophotovoltaic generation of electricity," *Jpn. J. Appl. Phys.* **39**, 1957–1961 (2000).
14. B. Bitnar, W. Durisch, J.-C. Mayor, H. Sigg, and H. R. Tschudi, "Characterization of rare earth selective emitters for thermophotovoltaic applications," *Sol. Energy Mater. Sol. Cells* **73**, 221–234 (2002).
15. J. G. Fleming, S. Y. Lin, I. El-Kady, R. Biswas, and K. M. Ho, "All-metallic three-dimensional photonic crystals with a large infrared bandgap," *Nature* **417**, 52–55 (2002).
16. M. U. Pralle, N. Moelders, M. P. McNeal, I. Puscasu, A. C. Greenwald, J. T. Daly, E. A. Johnson, T. George, D. S. Choi, I. El-Kady, and R. Biswas, "Photonic crystal enhanced narrow-band infrared emitters," *Appl. Phys. Lett.* **81**, 4685–4687 (2002).
17. D. L. C. Chan, M. Soljačić, and J. D. Joannopoulos, "Thermal emission and design in 2D-periodic metallic photonic crystal slabs," *Opt. Express* **14**, 8785–8796 (2006).
18. V. Rinnerbauer, Y. X. Yeng, W. R. Chan, J. J. Senkevich, J. D. Joannopoulos, M. Soljačić, and I. Celanovic, "High-temperature stability and selective thermal emission of polycrystalline tantalum photonic crystals," *Opt. Express* **21**, 11482–11491 (2013).

19. S. Maruyama, T. Kashiwa, H. Yugami, and M. Esashi, "Thermal radiation from two-dimensionally confined modes in microcavities," *Appl. Phys. Lett.* **79**, 1393–1395 (2001).
20. F. Kusunoki, J. Takahara, and T. Kobayasi, "Qualitative change of resonant peaks in thermal emission from periodic array of microcavities," *Electron. Lett.* **39**, 23–24 (2003).
21. H. Sai, Y. Kanamori, and H. Yugami, "High-temperature resistive surface grating for spectral control of thermal radiation," *Appl. Phys. Lett.* **82**, 1685–1687 (2003).
22. K. Ikeda, H. T. Miyazaki, T. Kasaya, K. Yamamoto, Y. Inoue, K. Fujimura, T. Kanakugi, M. Okada, K. Hatade, and S. Kitagawa, "Controlled thermal emission of polarized infrared waves from arrayed plasmon nanocavities," *Appl. Phys. Lett.* **92**, 021117 (2008).
23. H. T. Miyazaki, K. Ikeda, T. Kasaya, K. Yamamoto, Y. Inoue, K. Fujimura, T. Kanakugi, M. Okada, K. Hatade, and S. Kitagawa, "Thermal emission of two-color polarized infrared waves from integrated plasmon cavities," *Appl. Phys. Lett.* **92**, 141114 (2008).
24. G. Biener, N. Dahan, A. Niv, V. Kleiner, and E. Hasman, "Highly coherent thermal emission obtained by plasmonic bandgap structures," *Appl. Phys. Lett.* **92**, 081913 (2008).
25. I. Puscasu and W. L. Schaich, "Narrow-band, tunable infrared emission from arrays of microstrip patches," *Appl. Phys. Lett.* **92**, 233102 (2008).
26. X. Liu, T. Tyler, T. Starr, A. F. Starr, N. M. Jokerst, and W. J. Padilla, "Taming the blackbody with infrared metamaterials as selective thermal emitters," *Phys. Rev. Lett.* **107**, 045901 (2011).
27. J. A. Mason, S. Smith, and D. Wasserman, "Strong absorption and selective thermal emission from a midinfrared metamaterial," *Appl. Phys. Lett.* **98**, 241105 (2011).
28. M. N. Abbas, C.-W. Cheng, Y.-C. Chang, M.-H. Shih, H.-H. Chen, and S.-C. Lee, "Angle and polarization independent narrow-band thermal emitter made of metallic disk on SiO₂," *Appl. Phys. Lett.* **98**, 121116 (2011).
29. C. Wu, B. Neuner III, J. John, A. Milder, B. Zollars, S. Savoy, and G. Shvets, "Metamaterial-based integrated plasmonic absorber/emitter for solar thermo-photovoltaic systems," *J. Opt.* **14**, 024005 (2012).
30. S. Molesky, C. J. Dewalt, and Z. Jacob, "High-temperature epsilon-near-zero and epsilon-near-pole metamaterial emitters for thermo-photovoltaics," *Opt. Express* **21**, A98–A110 (2013).
31. C.-M. Wang and D.-Y. Feng, "Omnidirectional thermal emitter based on plasmonic nanoantenna arrays," *Opt. Express* **22**, 1313–1318 (2014).
32. H. T. Miyazaki, T. Kasaya, M. Iwanaga, B. Choi, Y. Sugimoto, and K. Sakoda, "Dual-band infrared metasurface thermal emitter for CO₂ sensing," *Appl. Phys. Lett.* **105**, 121107 (2014).
33. J. B. Pendry, A. J. Holden, D. J. Robbins, and W. J. Stewart, "Magnetism from conductors and enhanced nonlinear phenomena," *IEEE Trans. Microwave Theor. Tech.* **47**, 2075–2084 (1999).
34. N. I. Landy, S. Sajuyigbe, J. J. Mock, D. R. Smith, and W. J. Padilla, "Perfect metamaterial absorber," *Phys. Rev. Lett.* **100**, 207402 (2008).
35. X. Liu, T. Starr, A. F. Starr, and W. J. Padilla, "Infrared spatial and frequency selective metamaterial with near-unity absorbance," *Phys. Rev. Lett.* **104**, 207403 (2010).
36. K. Aydin, V. E. Ferry, R. M. Briggs, and H. A. Atwater, "Broadband polarization-independent resonant light absorption using ultrathin plasmonic super absorbers," *Nat. Commun.* **2**, 517 (2011).
37. J.-J. Greffet, R. Carminati, K. Joulain, J.-P. Mulet, S. Mainguy, and Y. Chen, "Coherent emission of light by thermal sources," *Nature (London)* **416**, 61 (2002).
38. B. J. Lee, C. J. Fu, and Z. M. Zhang, "Coherent thermal emission from one-dimensional photonic crystals," *Appl. Phys. Lett.* **87**, 071904 (2005).
39. W. Streier, S. Law, A. Rosenberg, C. Roberts, V. A. Podolskiy, A. J. Hoffman, and D. Wasserman, "Engineering absorption and black-body radiation in the far-infrared with surface phonon polaritons on gallium phosphide," *Appl. Phys. Lett.* **104**, 131105 (2014).
40. L. C. West and S. J. Eglash, "First observation of an extremely large-dipole infrared transition within the conduction band of a GaAs quantum well," *Appl. Phys. Lett.* **46**, 1156–1158 (1985).
41. T. Asano, K. Mochizuki, M. Yamaguchi, M. Chaminda, and S. Noda, "Spectrally selective thermal radiation based on intersubband transitions and photonic crystals," *Opt. Express* **17**, 19190–19202 (2009).
42. M. D. Zoysa, T. Asano, K. Mochizuki, A. Oskooi, T. Inoue, and S. Noda, "Conversion of broadband to narrowband thermal emission through energy recycling," *Nat. Photonics* **6**, 535–539 (2012).
43. T. Inoue, T. Asano, M. D. Zoysa, A. Oskooi, and S. Noda, "Design of single-mode narrow-bandwidth thermal emitters for enhanced infrared light sources," *J. Opt. Soc. Am. B* **30**, 165–172 (2013).
44. T. Inoue, M. D. Zoysa, T. Asano, and S. Noda, "Single-peak narrow-bandwidth mid-infrared thermal emitters based on quantum wells and photonic crystals," *Appl. Phys. Lett.* **102**, 191110 (2013).
45. T. Inoue, M. D. Zoysa, T. Asano, and S. Noda, "Filter-free nondispersive infrared sensing using narrow-bandwidth mid-infrared thermal emitters," *Appl. Phys. Express* **7**, 012103 (2014).
46. C. M. Watts, X. Liu, and W. J. Padilla, "Metamaterial electromagnetic wave absorbers," *Adv. Mater.* **24**, OP98–OP120 (2012).
47. T. Asano, S. Noda, T. Abe, and A. Sasaki, "Investigation of short wavelength intersubband transitions in InGaAs/AlAs quantum wells on GaAs substrate," *J. Appl. Phys.* **82**, 3385–3391 (1997).
48. C. Gmachl, H. M. Ng, and A. Y. Cho, "Intersubband absorption in GaN/AlGaIn multiple quantum wells in the wavelength range of 1.75–4.2 μm ," *Appl. Phys. Lett.* **77**, 334–336 (2000).
49. M. Imada, S. Noda, A. Chutinan, T. Tokuda, M. Murata, and G. Sasaki, "Coherent two-dimensional lasing action in surface-emitting laser with triangular-lattice photonic crystal structure," *Appl. Phys. Lett.* **75**, 316–318 (1999).
50. M. Imada, A. Chutinan, S. Noda, and M. Mochizuki, "Multidirectionally distributed feedback photonic lasers," *Phys. Rev. B* **65**, 195306 (2002).
51. J. D. Joannopoulos, S. G. Johnson, R. D. Meade, and J. N. Winn, *Photonic Crystals: Molding the Flow of Light* (Princeton University, 2008).
52. D. L. C. Chan, I. Celanovic, J. D. Joannopoulos, and M. Soljačić, "Emulating one-dimensional resonant Q-matching behavior in a two-dimensional system via Fano resonances," *Phys. Rev. A* **74**, 064901 (2006).
53. M. Ghebregbrhan, P. Bermel, Y. X. Yeng, I. Celanovic, M. Soljačić, and J. D. Joannopoulos, "Tailoring thermal emission via Q matching of photonic crystal resonances," *Phys. Rev. A* **83**, 033810 (2011).
54. T. Inoue, M. D. Zoysa, T. Asano, and S. Noda, "Realization of dynamic thermal emission control," *Nat. Mater.* **13**, 928–931 (2014).
55. D. Polder and M. V. Hove, "Theory of radiative heat transfer between closely spaced bodies," *Phys. Rev. B* **4**, 3303–3314 (1971).
56. K. Joulain, J.-P. Mulet, F. Marquier, R. Carminati, and J.-J. Greffet, "Surface electromagnetic waves thermally excited: Radiative heat transfer, coherence properties and Casimir forces revisited in the near field," *Surf. Sci. Rep.* **57**, 59–112 (2005).
57. L. Hu, A. Narayanaswamy, X. Chen, and G. Chen, "Near-field thermal radiation between two closely spaced glass plates exceeding Planck's blackbody radiation law," *Appl. Phys. Lett.* **92**, 133106 (2008).
58. S. Basu, Z. M. Zhang, and C. J. Fu, "Review of near-field thermal radiation and its application to energy conversion," *Int. J. Energy Res.* **33**, 1203–1232 (2009).
59. O. Ilic, M. Jablan, J. D. Joannopoulos, I. Celanovic, and M. Soljačić, "Overcoming the black body limit in plasmonic and graphene near-field thermophotovoltaic systems," *Opt. Express* **20**, A367–A384 (2012).
60. Y. Guo, C. L. Cortes, S. Molesky, and Z. Jacob, "Broadband super-Planckian thermal emission from hyperbolic metamaterials," *Appl. Phys. Lett.* **101**, 131106 (2012).